

Kinematics: A Clean Diagnostic for Separating Supernova Remnants from H II Regions in Nearby Galaxies

SEAN D. POINTS,¹ KNOX S. LONG,^{2,3,*} P. FRANK WINKLER,^{4,*} AND WILLIAM P. BLAIR^{5,*}

¹*National Optical Astronomy Observatory/Cerro Tololo Inter-American Observatory, Casilla 603, La Serena, Chile; spoints@ctio.noao.edu*

²*Space Telescope Science Institute, 3700 San Martin Drive, Baltimore MD 21218, USA; long@stsci.edu*

³*Eureka Scientific, Inc. 2452 Delmer Street, Suite 100, Oakland, CA 94602-3017*

⁴*Department of Physics, Middlebury College, Middlebury, VT, 05753; winkler@middlebury.edu*

⁵*The Henry A. Rowland Department of Physics and Astronomy, Johns Hopkins University, 3400 N. Charles Street, Baltimore, MD, 21218; wblair@jhu.edu*

(Received September 11, 2019; Revised October 15, 2019; Accepted March 13, 2024)

Submitted to ApJ

ABSTRACT

Many more supernova remnants (SNRs) are now known in external galaxies than in the Milky Way. Most of these SNRs have been identified using narrow-band imaging, separating SNRs from H II regions on the basis of [S II]:H α ratios that are elevated compared to H II regions. However, the boundary between SNRs and H II regions is not always distinct, especially at low surface brightness. Here we explore velocity structure as a possible criterion for separating SNRs from H II regions, using a sample of well-studied SNRs in the Large Magellanic Cloud (LMC) as well as a small number of SNRs in the galaxy M83. We find, perhaps not surprisingly, that even at large diameters, SNRs exhibit velocity broadening sufficient to readily distinguish them from H II regions. We thus suggest that the purity of most extragalactic samples would be greatly improved through spectroscopic observations with a velocity resolution of order 50 km s⁻¹.

Keywords: galaxies: individual (Large Magellanic Cloud) – galaxies: ISM – supernova remnants

1. INTRODUCTION

The study of extragalactic supernova remnants (SNRs) began modestly with the discovery of three radio candidates in the Large Magellanic Cloud (LMC) by Mathewson & Healey (1964), later confirmed through their radio and optical properties by Westerlund & Mathewson (1966). It was over a decade until SNR studies expanded to more distant galaxies through the optical identification of three remnants in M33 by D’Odorico et al. (1978). Great advances have been made since, so that today there are a total of over 1400 known SNRs (or at least strong candidates) in about a dozen galaxies, up to distances of ~ 10 Mpc—many times the number known in our own Galaxy (see Long 2017, for a recent discussion of the state of play in the field).

Unlike in the Galaxy, where most SNRs were first discovered through their radio properties and only about a third have even been detected optically (Green 2017), the vast majority of extragalactic remnants have been discovered optically. Some SNRs have been detected at X-ray and radio wavelengths in galaxies outside the Local Group, but due to limited sensitivity and angular resolution few were originally discovered in these wavelength bands. The classic method to identify SNRs optically is through the [S II]:H α ratio, where shock heated nebulae (primarily SNRs) typically have [S II]:H $\alpha \gtrsim 0.4$, compared with photoionized nebulae (H II regions and planetary nebulae) where [S II]:H α is typically $\lesssim 0.2$. This notable difference results from the fact that the gas behind shocks like those characterizing SNRs has a long cooling tail containing a range of low-ionization species, including S⁺, N⁺, and O⁰, while the photoionized gas surrounding hot stars is generally more highly ionized.

* Visiting astronomer, Cerro Tololo Inter-American Observatory, National Optical Astronomy Observatory, which is operated by the Association of Universities for Research in Astronomy (AURA) under a cooperative agreement with the National Science Foundation.

As larger telescopes and more sensitive instrumentation have enabled exploration of deeper extragalactic samples, the tidy [S II]:H α ratio criterion for distinguishing SNRs from H II regions has become blurred. At low surface brightness especially, photoionized regions such as the warm ionized medium in our Galaxy and the so-called diffuse ionized gas (DIG) in nearby galaxies can display [S II]:H α ratios that approach or exceed 0.4, as density decreases and the distance from the ionizing sources increases (e.g., [Haffner et al. 1999](#)). Hence, a patch of DIG in a nearby galaxy may be misidentified as a potential low-surface-brightness SNR. Also, extragalactic SNRs may be embedded in complex emission regions or located so close to regions of H II emission that they cannot be resolved with ground-based facilities. Intrinsic observational uncertainty in the derived line ratios for faint emission-line objects can also cause ambiguity for objects with observed ratios near the 0.4 threshold. Therefore, it would be valuable to have an additional optical diagnostic for positive identification of SNRs; hence the motivation for this study.

A potential diagnostic for SNRs is to take advantage of the fact that the material behind a SNR shock will have bulk motions comparable to the local shock speed, several hundred km s⁻¹, whereas material in H II regions will for the most part have velocities of order 10 km s⁻¹. Unfortunately, although spectroscopic follow-up of a large number of the nebulae identified as SNRs in extragalactic surveys has taken place (e.g., [Matonick & Fesen 1997](#); [Blair & Long 1997](#); [Gordon et al. 1998](#); [Lee & Lee 2014a,b](#); [Lee et al. 2015](#); [Winkler et al. 2017](#); [Long et al. 2018, 2019](#)), most of these spectroscopic surveys have not had sufficient spectral resolution to measure the expected line broadening in SNRs and use it as a meaningful diagnostic.

Here we report a survey of selected SNRs in the LMC, along with a few SNR candidates in M83, to test whether measuring line broadening is a practical way to separate SNRs from H II regions, and to assess what additional information line broadening may provide in attempting to understand the nature of SNRs in our sample. The LMC, with 59 SNRs and 15 additional candidates, is the obvious place to carry out such a study because it has the most fully characterized sample of SNRs of any galaxy (see, e.g. [Maggi et al. 2016](#); [Bozzetto et al. 2017](#)). There is, however, one obvious observational difference between the SNRs in the LMC and those in other more distant galaxies: at 50 kpc ([Pietrzyński et al. 2013](#)), the SNRs in the LMC are fully resolved, and simple long-slit spectroscopy samples only a small portion of each SNR. This is in contrast to the situation in a galaxy like M83 ($d = 4.6$ Mpc, [Saha et al. 2006](#)), where a spectroscopic aperture (slit or fiber) typically samples most or all of an SNR. To address this situation, we obtained spectra of several SNRs and a few H II regions in the LMC by scanning the slit over the entire object, thus obtaining an integrated spectrum analogous to what a slit might encompass for an object in a galaxy like M83.

In the following sections, we detail our new kinematic observations of SNRs, present our results, and then provide a discussion of our findings. A brief summary of our conclusions appears at the end.

2. OBSERVATIONS AND DATA REDUCTION

We used the Goodman High-Throughput Spectrograph (GHTS, [Clemens et al. 2004](#)) at the SOAR 4.1-m telescope on Cerro Pachón to measure the velocity broadening of emission lines as a potential diagnostic of SNRs. Our observations took place on five nights: 2018 Dec 14-16 and 2019 Jan 15-16 (UT), as detailed in Table 1. We used the Goodman Red Camera, equipped with a 4096×4112 pixel back-illuminated, deep-depletion, astro-multi-2 coated e2v 231-84 CCD, and chose the red-optimized 1200 lines mm⁻¹ Volume Phased Holographic (VPH) grism for our observations. At a central wavelength of 6840 Å, the total wavelength coverage was 6230–7460 Å, which included lines of interest such as [O I] $\lambda\lambda$ 6300, 6363, [N II] $\lambda\lambda$ 6548, 6583, H α , and [S II] $\lambda\lambda$ 6716, 6731. We used a 0''.6 slit with 1×1 pixel binning as the optimum compromise between resolution and throughput. The instrumental profile, as measured from the HgAr + Ne calibration lamp lines was 3.95 ± 0.17 pixels (≈ 1.2 Å; ≈ 53 km s⁻¹). The spatial scale along the slit was 0''.15 pixel⁻¹.

We obtained spectra toward a sample of LMC and M83 SNRs and H II regions. For the primary LMC targets, we used a drift-scan technique, allowing the narrow slit to scan gradually across the entire source. This enabled us to sample the full range of filamentary velocities, somewhat analogous to the situation for long-slit spectra toward M83 and other more distant galaxies, where much or all of a marginally resolved source falls within the slit. We selected the LMC targets based on the criteria of size and surface brightness. We chose targets that were small enough (in either the N-S and/or E-W direction) to be covered in a single scan with the 3''.9 long Goodman slit, with at least some margin at one or both ends to facilitate sky subtraction. For simplicity, the slit was aligned either N-S or E-W so we could scan along a single coordinate perpendicular to the slit.

We used flux-calibrated images from the Magellanic Clouds Emission Line Survey (MCELS, [Smith & MCELS Team 1999](#); [Winkler et al. 2015](#); [Paredes et al. 2015](#)) to estimate the total H α flux and surface brightness of SNRs in the LMC. Ideally, for this experiment we would have chosen examples covering the full range from brightest to faintest.

However, because drift-scan spectra are “inefficient,” in that much of what the slit sees as it scans over an object is blank sky rather than filaments of emission, we discovered that it was not practical to observe the fainter objects with this technique.

With the Goodman spectrograph, it is quite easy to switch between imaging and spectrographic modes. In order to facilitate both the setups and subsequent analysis, we obtained short direct images in $H\alpha$, SDSS r' , and in some cases [S II] as well, before the scanned spectra for each object.

In addition to the scanned spectra, we also obtained long-slit spectra for five of the LMC SNRs in our sample, in order to assess the effectiveness of the scans compared with more traditional long-slit spectra. The positions and position angles for these long-slit observations were chosen to minimize stellar contamination while maximizing coverage of the SNR emission regions. Finally, for comparison with the situation typical for more distant galaxies, we also used the same setup to obtain long-slit spectra at two positions in the galaxy M83, chosen to include multiple SNRs from the Blair et al. (2012) catalog. (One or more H II regions also lay along each slit position.) Table 1 gives a journal of all our observations of LMC and M83 targets. In total, we obtained drift-scan spectra toward 15 LMC SNRs and eight LMC H II regions (three explicitly targeted and five others covered in SNR scans) plus long-slit spectra of five LMC SNRs, five M83 SNRs, and three M83 H II regions.

After obtaining the spectra for each object, we took comparison lamp spectra using HgAr + Ne lamps for wavelength calibration. For flux calibration, we observed several spectrophotometric standard stars from the list of Hamuy et al. (1992, 1994) at the beginning and/or end of each night.

We used common IRAF¹ tasks to perform the basic data reductions, including bias-subtraction, trimming, and flat-fielding (using dome flats obtained during the day), for both the drift-scan and long-slit 2-D spectra.

Because the overall exposure time for most of our targets was more than 1800 s, we investigated the wavelength stability of the data for each object by looking for differences in the centroids of telluric emission lines. The positions of the telluric lines in the object spectrum taken closest in time to the corresponding comparison lamp spectrum were used as the fiducial values. If the telluric emission lines in another spectrum of that object were not well aligned with the fiducial spectrum, we determined the pixel offset between that spectrum and the fiducial, shifted the spectrum to match the fiducial, and combined the individual spectra. After all the spectra for a given object had been aligned and combined, we used the comparison spectra and IRAF tasks in the `twodspec.longslit` package to rectify each 2-D spectrum to a linear wavelength scale.

We also derived a wavelength solution for the all the standard star spectra, combined these for each night, and determined a nightly sensitivity function, which we applied to all the object spectra for that night. Finally, for each object, we then used the IRAF task `background` to subtract the night-sky emission, selecting as background the portion(s) of the slit that fell outside the target object.

¹ IRAF is distributed by the National Optical Astronomy Observatory, which is operated by the Association of Universities for Research in Astronomy (AURA) under a cooperative agreement with the National Science Foundation.

Table 1. SOAR Goodman Observation Log

Object ^a	Other Names ^b	R.A. ^c	Decl. ^c	Obs. Date	Slit PA ^d	Exposure	Mode ^e	Scan Rate
		(J2000)	(J2000)	(UT)	(deg)	(s)	Scan/LS	(" hr ⁻¹)
LMC SNRs:								
N4	J0453-6655	04:53:14.0	-66:55:10	2018-12-16	0	2x1800	Scan	400
N11L	J0454-6625	04:54:49.9	-66:25:36	2018-12-15	0	3x1800	Scan	122
		04:54:50.7	-66:25:50	2019-01-15	43	2x900	LS	0
N86	J0455-6839	04:55:43.7	-68:39:02	2018-12-14	90	3x1200	Scan	400
		04:55:42.8	-68:38:06	2019-01-16	74	2x1000	LS	0
N103B	J0508-6843	05:08:59.4	-68:43:35	2018-12-14	0	3x1200	Scan	60
N120	J0518-6939	05:18:43.5	-69:39:11	2018-12-16	0	3x1200	Scan	225
		05:18:51.0	-69:39:13	2018-12-16	14	2x600	LS	0
B0520-69.4	J0519-6926	05:19:45.3	-69:26:01	2019-01-15	90	3x1800	Scan	280
		05:19:46.8	-69:25:38	2019-01-15	100	2x1200	LS	0
N132D	J0525-6938	05:25:02.7	-69:38:33	2019-01-16	90	2x1800	Scan	210
N49B	J0525-6559	05:25:24.9	-65:59:18	2018-12-14	0	3x1200	Scan	110
		05:25:24.9	-65:59:18	2019-01-16	328	2x900	LS	0
N49	J0526-6605	05:26:00.1	-66:05:00	2018-12-14	0	3x600	Scan	600
DEM-L205	J0528-6726	05:28:11.1	-67:26:49	2018-12-16	0	3x1800	Scan	500
N206	J0531-7100	05:31:57.9	-71:00:16	2018-12-16	0	2x1800	Scan	350
N63A	J0535-6602	05:35:43.8	-66:02:13	2018-12-14	90	3x1200	Scan	135
N59B	J0536-6735	05:36:04.2	-67:35:11	2018-12-15	0	3x1200	Scan	375
DEM-L316B	J0547-6943	05:47:00.0	-69:42:50	2019-01-16	0	3x1800	Scan	320
DEM-L316A	J0547-6941	05:47:20.9	-69:41:27	2018-12-15	0	3x1800	Scan	160
LMC H II regions:								
N80	-	04:54:12.6	-68:21:51	2019-01-15	90	3x1000	Scan	165
N38	-	05:20:32.9	-66:46:46	2019-01-16	0	2x1200	Scan	210
HII(N132D)-E	-	05:25:02.7	-69:38:33	2019-01-16	90	2x1800	Scan	210
HII(N132D)-W	-	05:25:02.7	-69:38:33	2019-01-16	90	2x1800	Scan	210
HII(N49B)	-	05:25:24.9	-65:59:18	2018-12-14	0	3x1200	Scan	110
HII(N63A)	-	05:35:43.8	-66:02:13	2018-12-14	90	3x1200	Scan	135
HII(N59B)	-	05:36:04.2	-67:35:11	2018-12-15	0	3x1200	Scan	375
N175	-	05:40:43.0	-70:02:30	2018-12-15	0	2x1200	Scan	450
M83 Objects:								
B12-023	B04-07,S03-007	13:36:48.3	-29:51:45	2019-01-15	96	2x1800	LS	0
B12-039	B04-11	13:36:50.3	-29:52:47	2019-01-15	96	2x1800	LS	0
B12-180	B04-58,S03-109	13:37:07.5	-29:51:33	2019-01-16	96	3x1500	LS	0
B12-191	B04-53,S03-105	13:37:08.6	-29:51:35	2019-01-16	96	3x1500	LS	0
B12-208	B04-41,S03-081	13:37:11.7	-29:51:39	2019-01-16	96	3x1500	LS	0
M83-HII-1	-	13:36:48.0	-29:52:44	2019-01-15	96	2x1800	LS	0
M83-HII-2	D83-13	13:36:52.9	-29:52:51	2019-01-15	96	2x1800	LS	0
M83-HII-3	M06-34	13:37:01.4	-29:51:26	2019-01-16	96	3x1500	LS	0

^a N: [Henize \(1956\)](#) identifications; DEM: [Davies et al. \(1976\)](#); B12: [Blair et al. \(2012\)](#); HII: H II emission sections extracted from locations along the long slits.

^b J#: as listed by [Bozzetto et al. \(2017\)](#); B04: [Blair & Long \(2004\)](#); S03: [Soria & Wu \(2003\)](#) X-ray source number; D83: [de Vaucouleurs et al. \(1983\)](#); M06: [Maddox et al. \(2006\)](#) radio source.

^c Object center position adopted from that of [Bozzetto et al. \(2017\)](#) for scans; slit center position for long slits; object coordinates for M83 objects.

^d Astronomical position angle (east from north) of long dimension of slit.

^e Scan = scanned spectrum; LS = Long-slit.

3. RESULTS AND ANALYSIS

Figures 1 and 2 provide representative examples of the spectroscopic and imaging data we obtained toward the LMC SNR sample. The upper panel of Figure 1 shows the $H\alpha$ image of the SNR N86 obtained by the Goodman using its direct imaging mode, where the blue dashed rectangle outlines the area scanned in spectroscopic mode. Figure 2 shows the $H\alpha$ image of the LMC SNR B0520–69.4, before (left) and after (right) continuum subtraction. One has no difficulty identifying N86 because of its relatively high surface brightness filaments and its location in a sparse field on the western edge of the LMC. However, the crowded star field and the relatively low surface brightness of the emitting filaments in SNR B0520–69.4 (see Fig. 2 top) make it more difficult to identify its structure until after continuum subtraction.

The background-subtracted 2-D spectra of N86 and B0520–69.4 (lower panels of Figures 1 and 2, respectively) reveal complex kinematic structure, despite the crowded star field in the latter case. Both of these show multiple red- and blue-shifted components, especially near the slit centers that tracked across the central part of the objects, where we expect the line-of-sight velocities to be highest. Such complex structure is seen in virtually all of our scanned data for LMC SNRs.

While the 2-D spectra are necessary to reveal the full complexity of the velocity structure, it is also useful to extract 1-D spectra from the scanned data in order to provide a single quantitative measure for the velocity broadening. The 1-D spectra from LMC objects also provide a direct comparison with spectra from SNRs and other objects in M83 and other more distant galaxies. Therefore, for each of the scanned spectra, we summed over all the lines containing the object, omitting small regions where bright stars crossed the slit. In four of the spectra of our LMC primary targets (N49B, N59B, N63A, and N132D) we also detected a second component attributable to nearby diffuse $H\alpha$ emission. In these cases we extracted 1-D spectra for both the SNR and H II region components separately.

Figure 3 shows examples of extracted 1-D spectra from B0520–69.4. The lower trace shows the extracted spectrum from the scanned observation (lower panel of Fig. 2), while the upper trace is from the position of the slit indicated on the upper panels of Fig. 2. The scanned data clearly reveal a more complex velocity structure and broader emission lines with multiple peaks than does the long-slit spectrum. The same is true for the other objects observed in both scanned and long-slit modes, as shown in Table 2.

For the two slit positions we observed in M83, each object crossed by the slit (SNRs and serendipitous H II regions) extended over only a few lines ($\lesssim 2''$) along the slit. Here we simply summed over the relevant lines to obtain the 1-D spectra. Several examples of the extracted spectra from LMC and M83 SNRs and H II regions are shown in Figures 4 and 5, respectively. The extracted 1-D spectra from the scanned LMC SNR sample and from the M83 long-slit SNR sample both show the same general pattern of emission lines that are broadened in comparison to those in the spectra of H II regions.

To obtain a quantitative comparison between SNRs and H II regions, we determined the spectral widths of the emission lines in our sample using two different methods for both the scanned and long-slit data. In the first method we simply measured the widths of the lines at 20% of the peak value, while for the second we fit each of the principal lines in the spectra— $H\alpha$, the [N II] doublet, and the [S II] doublet—with simple, single-component Gaussians. Simply measuring the width of the profile at a particular percentage of the peak has the advantage that it is relatively insensitive to asymmetries in the profiles, but it is quantized at the scale of an individual pixel. Gaussian fits do not suffer from this limitation; they readily give measures for the total flux in the lines; and they make comparisons with spectra obtained from different instruments more straightforward. In Table 2, we present the 20% results only for $H\alpha$, while we tabulate the FWHM results for all three lines, both for SNRs and H II regions. As expected, the $H\alpha$ 20% widths are larger than the FWHM values for individual objects, and the 20% widths are significantly higher for SNRs than for H II regions.

Table 2. Extracted Fluxes and Line Widths

Object	Mode	H α	H α	H α	[N II]	[N II]	[S II]	[S II]	L _{Hα} ^d
	Scan/LS	Flux ^a	(FWHM) ^b	(20% Width) ^c	Flux ^a	(FWHM) ^b	Flux ^a	(FWHM) ^b	
			(Å)	(Å)		(Å)		(Å)	
LMC SNRs:									
N4	Scan	23.00	2.35	3.62	4.03	2.39	13.90	2.39	22.8
N11L	Scan	35.60	2.83	4.53	7.09	2.89	26.90	2.78	10.8
	LS	90.50	2.59	3.63	17.10	2.63	66.80	2.50	–
N86	Scan	62.00	2.40	3.93	11.20	2.46	45.40	2.30	41.1
	LS	108.00	1.87	3.02	16.70	1.80	68.50	1.87	–
N103B	Scan	43.30	4.03	5.44	7.57	4.53	11.99	3.90	4.3
N120	Scan	190.00	1.67	2.72	36.30	1.87	96.80	2.75	70.8
	LS	114.00	1.94	3.02	29.00	1.94	107.50	2.04	–
B0520-69.4	Scan	18.70	4.94	6.04	6.24	4.65	17.78	4.54	13.0
	LS	9.58	1.55	2.42	2.25	1.59	6.05	1.58	–
N132D ^e	Scan	28.10	1.56	2.42	5.94	1.58	15.50	1.40	14.8
N49B	Scan	27.90	5.58	5.44	9.82	3.81	14.30	4.61	5.1
	LS	31.70	5.83	5.43	16.00	4.86	19.90	4.78	–
N49	Scan	468.00	5.28	7.22	106.00	5.52	355.00	5.03	232.0
DEML-205	Scan	189.00	1.66	2.72	27.30	1.64	71.40	1.82	235.0
N206	Scan	55.30	1.63	2.42	12.10	1.85	44.00	2.56	48.1
N63A	Scan	149.00	2.21	3.93	26.70	2.34	128.80	1.88	33.3
N59B	Scan	67.30	1.88	2.72	10.20	1.81	32.40	1.87	41.8
DEM-L316B	Scan	27.70	4.28	5.76	4.54	4.72	27.50	4.50	22.0
DEM-L316A	Scan	32.70	3.73	3.93	5.54	4.07	27.50	3.48	13.0
LMC H II Regions:									
N80	Scan	74.30	1.11	1.81	9.49	1.24	15.18	1.28	16.9
N38	Scan	297.00	1.27	1.81	22.70	1.18	33.50	1.17	103.0
HII(N132D)-E	Scan	3.09	1.34	2.11	0.54	1.19	1.17	1.21	1.6
HII(N132D)-W	Scan	2.56	1.30	2.11	0.62	1.16	1.32	1.16	1.3
HII(N49B)	Scan	26.90	1.18	1.81	6.27	1.18	17.11	1.12	4.9
HII(N63A)	Scan	70.80	1.20	1.81	7.94	1.11	10.84	1.15	15.8
HII(N59B)	Scan	351.00	1.53	2.11	33.50	1.52	78.70	1.58	218.0
N175	Scan	130.00	1.25	1.81	15.30	1.15	26.70	1.16	96.9
M83 Objects:									
B12-023	LS	1.79	3.66	5.43	1.89	5.40	1.78	5.54	–
B12-039	LS	4.06	1.59	2.41	2.74	1.83	2.45	1.94	–
B12-180	LS	0.77	2.87	4.83	1.16	3.99	0.97	4.05	–
B12-191	LS	0.48	2.14	4.22	0.70	3.52	0.50	2.89	–
B12-208	LS	0.27	1.67	2.71	0.29	3.52	0.26	3.39	–
M83-HII-1	LS	25.90	1.53	2.41	7.96	1.39	4.64	1.46	–
M83-HII-2	LS	3.67	1.19	1.81	1.42	1.10	0.58	1.11	–
M83-HII-3	LS	0.52	1.35	2.11	0.22	1.45	0.12	1.32	–

^a Fluxes are in units of 10^{-15} ergs cm⁻² s⁻¹. [N II] flux is for $\lambda 6583$ only while [S II] flux is total for the doublet. Note that these do *not* represent the total flux from the entire object, but for scans is an average flux through the slit as it moved across the object. For long-slit spectra, these are simply the total flux through the fixed 0''.6 slit. See text, section 4.2.

^b Single Gaussian FWHM values in Å; [N II] is for $\lambda 6583$ and [S II] is for $\lambda 6716$; see text.

^c Line widths at 20% of peak value, in Å; see text.

^d The H α luminosities are in units of 10^{35} ergs s⁻¹.

^e N132D is embedded in a region of strong H II emission, which gives a strong narrow component to the lines, producing artificially narrow Gaussian fits. Fainter broad emission is evident in both the 2-D and 1-D spectra (see Fig. 4).

From the data presented in Table 2, we conclude the following:

- In general the H II regions have narrower line profiles than do the SNRs. This can be seen qualitatively in Figs 4 & 5 where the emission lines in the SNRs are broader than the emission lines in the H II regions. In Figure 6, we plot the spread of values for the FWHM from the $H\alpha$ line for the scanned LMC SNRs and H II regions and the long-slit data of M83 SNRs and H II regions. As seen in this figure, the H II region line profiles are close to the instrumental resolution of 1.2 \AA . Therefore, with sufficiently high spectral resolution, it is easy to separate the H II regions from the SNRs (see §4.1 for details).
- The FWHM and 20% widths of the $H\alpha$ line give similar results and are correlated, as seen in Table 2 and in the left-hand side of Figure 7. In general the FWHM of the $H\alpha$ line is smaller than the 20% width of the $H\alpha$ line. Hence, even though the Gaussian fits to the line profiles do not capture the full complexity, and in some case extent, of the line profiles, they can be used effectively to discriminate between H II regions and SNRs.
- Our experiments with long-slit spectra make it clear that the kinematic distinction between SNRs and H II regions is less effective when observing single positions of spatially-resolved SNRs in long-slit mode than it is when observing the entire SNR (cf. Fig. 3). This is probably what one would have expected *a priori*, since one generally selects slit positions to overlay the brightest portion of a SNR, often along the rim with high surface brightness but relatively low line-of-sight shock velocity.
- For the LMC SNRs, the FWHM of $H\alpha$ and other lines are comparable (see Fig 7); however, in M83 there is a clear tendency for the [S II] and [N II] line widths to be greater than those of $H\alpha$, indicative of contamination of the $H\alpha$ line by adjacent or overlying photoionized emission that could not be accurately subtracted. This indicates that velocity broadening of forbidden lines may be the preferred diagnostic in galaxies beyond the Local Group.

4. DISCUSSION

We have obtained drift-scan spectra toward 15 SNRs and eight H II regions in the LMC in addition to long-slit spectra of five SNRs and three H II regions in M83. We scanned across the LMC targets in order to measure the integrated line profiles of the SNRs and H II regions so that we can compare the results to the measured properties of SNRs and H II regions in more distant galaxies where objects can be centered in a single long-slit spectrum. Below we discuss our results in detail.

4.1. LMC H II Regions versus SNRs

We obtained the scanned data to obtain integrated spectra to investigate the possibility that velocity broadening of emission lines may be used to discriminate between SNRs and H II regions in distant galaxies. As seen in Table 2, the FWHM of simple, single-component Gaussians toward LMC H II regions ranges between $1.1\text{--}1.5 \text{ \AA}$ for the $H\alpha$ line, $1.1\text{--}1.5 \text{ \AA}$ for the [N II] 6583 \AA line, and $1.1\text{--}1.6 \text{ \AA}$ for the [S II] 6716 \AA line. These values are close to the instrumental profile of 1.2 \AA for our Goodman spectrograph configuration.

For the scanned data on LMC SNRs, we see that the FWHM of the emission lines varies between $1.6\text{--}5.6 \text{ \AA}$ in $H\alpha$, $1.6\text{--}5.5 \text{ \AA}$ for the 6583 \AA [N II] line, and $1.8\text{--}5.0 \text{ \AA}$ for the 6716 \AA [S II] line.² In general, the FWHMs of the emission-lines seen in the scanned SNR spectra are greater than the FWHM of those lines in LMC H II regions and significantly broader than the instrumental profile of 1.2 \AA .

Even though we see some outliers in the SNR line profiles, it is clear that we systematically see velocity broadening in the SNRs in comparison with the H II regions. This is true despite the fact that we did not observe at high enough resolution to actually resolve the H II region emission lines, which should be in the $10\text{--}20 \text{ km s}^{-1}$ range ($\approx 0.2\text{--}0.5 \text{ \AA}$). One expects bulk motions, even in older SNRs nearing the end of their radiative phase, of at least 50 km s^{-1} . While some of this motion will be in the plane of the sky, by observing the entire emission from a given object, we see sufficient bulk motion along the line-of-sight to broaden the lines in the SNRs. Hence, observations at $\sim 50 \text{ km s}^{-1}$ resolution appear to be sufficient to be a good diagnostic of shocks versus photoionization.

² Formal Gaussian fits to the N132D spectrum give somewhat narrower values, due to “contamination” from the strong H II emission in which the SNR is embedded. However, a much broader component for all these lines is evident in the spectrum (see Fig. 4).

We note in passing that $[\text{S II}]:\text{H}\alpha$ is $\lesssim 0.4$ in the scanned spectra of both N103B (0.27) and DEML205 (0.38). Both are well-established as SNRs, and both have velocity widths that are significantly broader than H II regions despite the lower ratios. While long-slit spectra may show individual filaments in these objects have higher $[\text{S II}]:\text{H}\alpha$ ratios than these global averages, the scanned spectra are more representative of the situation in more distant galaxies where long slit spectra cover much if not all of the SNR.

To assess the robustness of our conclusion that velocity broadening is a good way to separate SNRs from H II regions in our sample of LMC and M83 objects, we performed an Anderson-Darling k-sample test on the measured FWHMs of the H II regions and SNRs. Specifically, we tested whether it was possible that the FWHMs of nebular lines of the H II regions and SNRs could arise from the same distribution. In testing, we used the measured FWHMs of the scanned spectra of LMC objects and the long-slit spectra of M83 objects. Regardless of whether we considered $\text{H}\alpha$, $[\text{N II}]$, or $[\text{S II}]$ lines for the test, we found that the probability (p-value) that the samples were drawn from a common distribution was $\ll 0.001$, confirming that the quality and velocity resolution of our data is sufficient to show that the FWHMs of emission lines from SNRs and H II regions are distinct.

4.2. Integrated Line Flux Measurements and Luminosity Comparison with Other Galaxies

For our spectra scanned over entire objects, we have the opportunity to obtain *integrated* line fluxes, and corresponding luminosities, for SNRs in the LMC. After sky subtraction and extraction of 1-D spectra for each object, we obtained the integrated flux in $\text{H}\alpha$ (and other lines). But since only a small fraction of the emitting region lies within the slit at any time during the scan, we must then divide by an “inefficiency factor”: $(\text{slit area})/(\text{scan area}) = (\text{slit width})/(\text{scan distance})$. For example, for N4 the $0.6''$ slit scanned at $400'' \text{ hr}^{-1}$ during exposures of 1800 s (Table 1), so the fraction of the scan covered at any instant is $0.6''/200'' = 0.003$. The results for the 15 LMC SNRs with scanned spectra are given in Table 2. We measure $\text{H}\alpha$ luminosities from 4×10^{35} to $2.4 \times 10^{37} \text{ erg s}^{-1}$ (assuming a distance of 50 kpc and no absorption).

As a check on these values, in Figure 8 we compare them with those obtained by summing over regions containing the SNRs in narrow-band $\text{H}\alpha$ mosaic images of the LMC from MCELS (Smith & MCELS Team 1999; Paredes et al. 2015). (As noted above, we used these images in selecting targets for scanned spectra.) We find that fluxes (and luminosities, of course) are fairly well correlated in these two independent data sets, though the MCELS image-based values are typically larger than those from scanned spectra by about a factor of 2. This can be attributed to at least three factors: (1) the MCELS $\text{H}\alpha$ filter was broad enough (FWHM 30 Å) to transmit $[\text{N II}]$ emission at the $\sim 30\%$ level, contaminating the $\text{H}\alpha$ emission; (2) the regions measured in the MCELS images included somewhat more emission than what was covered in the Goodman spectrograph scans; and (3) the presence of non-uniform diffuse $\text{H}\alpha$ emission toward the SNRs complicated sky-subtraction such that the sky-background was never completely removed. Each of these three effects would produce an over-estimate of the MCELS-derived $\text{H}\alpha$ luminosities of the SNRs in comparison to the values determined using the scanned Goodman data.

It is interesting to compare these values with those for more distant galaxies, where the integrated fluxes have been obtained through narrow-band imaging and/or through long-slit spectra.³ For SNRs in M33, Long et al. (2010) measured $\text{H}\alpha$ fluxes using narrow-band images from the Local Group Galaxies Survey (LGGS, Massey et al. 2007), and found values up to a maximum of $2.7 \times 10^{37} \text{ erg s}^{-1}$. Lee & Lee (2014a) also used $\text{H}\alpha$ images from the LGGS to do similar luminosity measurements for M31, where they found SNRs (and candidates) to have $\text{H}\alpha$ luminosities up to $1.0 \times 10^{37} \text{ erg s}^{-1}$.

For M83, SNR line fluxes have been measured both in narrow-band images from Magellan (Blair et al. 2012) and in multi-slit spectra from Gemini-S (Winkler et al. 2017). As Fig. 5 of the latter paper shows, there is a tight correlation between the two data sets; the vast majority of objects have $\text{H}\alpha$ fluxes from imaging between 1 and 2 times those measured from spectra. The luminosities for M83 SNRs range up to $\sim 5 \times 10^{37} \text{ erg s}^{-1}$, a few times brighter than the most luminous ones in M31 or M33. This is probably attributable to the fact that active star formation is taking place in M83, with an attendant higher mean ISM density compared with the more quiescent M31 or M33 (Winkler et al. 2017).

Within the context of these three much larger galaxies, we see that the brightest SNRs in the LMC have luminosity higher than those in M31, comparable with those in M33, and a factor of about two lower than those in M83. We note, however, that we do *not* present a complete luminosity function for LMC SNRs, for we have sampled only about

³ Neither of these methods are ideal: narrow-band images through most “ $\text{H}\alpha$ ” filters pass some or all of the $[\text{N II}] \lambda\lambda 6548, 6583$ line flux, while typical long slits admit only a fraction of the light from all but the smallest objects.

25% of them. Since we intentionally selected objects with high surface brightness, our sample should be at least close to the bright end of the luminosity function; however, there may be other high-luminosity objects that we did not include because they are too large to be covered by the 3/9 Goodman slit. Nevertheless, we can conclude that the brightest SNRs in the LMC have luminosities that at least approach those in M83.

4.3. Comparison with M83 SNRs and H II regions

At the distance of M83 (4.6 Mpc), $1''$ corresponds with about 22 pc, so our $0.6''$ slit width corresponds to ~ 13 pc. This is large enough to engulf the majority of flux from small objects that are well-centered on the slit, but does not get all of the flux from some objects whose diameters range upwards of 20 pc, as is the case for a few of the objects observed. Seeing effects could also cause some light to be lost from the narrow slit.

Nonetheless, comparison of the kinematics for the small number of M83 SNRs in Table 2 with the randomly sampled H II regions that were observed serendipitously along the same slits, we see that all of the SNRs observed show significant broadening above that seen for H II regions. For two objects, B12-039 and B12-208, the shock broadening is subtle in the $H\alpha$ measurements, but is more clear from the other listed lines. This is an indication that overlying diffuse or contaminating $H\alpha$ emission may be influencing the observed $H\alpha$ despite our attempts to subtract it. Objects B12-023, -180, and -191 are clearly broadened in all three listed lines, although again, one can see a systematic effect where the broadening is higher in [N II] and [S II] than in $H\alpha$. This indicates that using lines other than $H\alpha$ may be the most effective application of the new kinematic technique when observing more distant galaxies, especially as the technique is applied to even fainter objects where correcting for $H\alpha$ contamination may be even more of a problem.

4.4. Line Widths and Shock Models

In addition to being a discriminant between H II regions and SNRs, higher resolution observations also communicate something about the SNR itself. The LMC SNRs we have observed range in diameter from approximately 6.8 pc in the case of N103B to nearly 60 pc in the case of N86. Analysis of the X-ray spectrum of N103B suggests it is a relatively young, 860-year-old SNR produced by a thermonuclear explosion (Hughes et al. 1995), while N86 is an old SNR, dominated by emission from swept-up interstellar material, with an age of perhaps 53,000 years (Williams et al. 1999). Given this, it is not surprising that the widths of the lines in N103B are greater than in N86. However, as shown in Fig. 9, any trends of line width with diameter or age are fairly weak. All very large diameter, very old SNRs do have fairly narrow line widths, but objects with diameters $\lesssim 30$ pc and ages $\lesssim 10,000$ years show a large range in observed line widths.

On the other hand, it is important to remember that at 6500 Å, a velocity of 300 km s^{-1} corresponds to 6.5 Å , so the velocity widths we observe are far less than the primary shock velocity (especially for the young objects), even if one allows for the fact that the FWHM is less than the full widths at zero intensity. Qualitatively, we can understand this as follows: Consider a SNR with a primary shock velocity of 1000 km s^{-1} expanding into an ISM with a mean density of 1 cm^{-3} . The primary shock will be non-radiative, i.e., material behind the shock will not have had time to cool to $\sim 10,000 \text{ K}$, as needed to produce bright $H\alpha$ and the forbidden lines typically observed in optically identified SNRs. There are SNRs where these fast shocks are observed, the so-called Balmer-dominated SNRs (see, e.g. Heng 2010).⁴ In these, the only observed optical radiation arises from H atoms undergoing ionization, since the temperature behind the shock is 10^7 K or more. A few such SNRs do exist in the LMC, but they are faint and are not among the ones we have observed. Furthermore, objects such as these are too faint to be observed in more distant galaxies.

In a typical SNR, the optical emission we detect arises as the primary shock drives secondary shocks into clouds with densities of 10-100 times that of the average ISM. The pressure behind these secondary shocks will be in approximate equilibrium with that of the primary shock, that is $v_2 \sim \sqrt{(n_1/n_2)} v_1$ or 100 to 300 km s^{-1} . The initial temperature behind these shocks is still rather high, of order 10^6 K , but at these temperatures and densities the shocked gas will cool relatively quickly to the point where it produces significant amounts of $H\alpha$ and forbidden-line radiation. So except in cases where we are viewing the ejecta directly, as in Cas A, we do not expect the lines to be much broader than we have observed here.

5. SUMMARY/CONCLUSIONS

⁴ N103B does have Balmer-dominated filaments (Ghavamian et al. 2017), but the bulk of the radiation arises from radiative shocks.

Large numbers of SNRs have been and are continuing to be identified in nearby galaxies using ratios derived from narrow-band filter imaging to distinguish SNRs from the principal source of contamination, i.e. H II regions. Because all of the SNRs in a nearby galaxy lie at essentially the same distance and because absorption along the line-of-sight is generally low and less variable than in the plane of the Galaxy, such samples are important for understanding the class properties of SNRs. To carry out such studies accurately, however, one must be sure that the sample is not contaminated by objects that are not SNRs. Here we suggest that one very clear way to eliminate imposters from a sample is to take spectra with sufficient spectral resolution ($\sim 50 \text{ km s}^{-1}$) to separate SNRs from H II regions.

To test this suggestion, we have obtained spectra of 15 SNRs and of 8 H II regions in the LMC with the SOAR telescope with a spectral resolution of 53 km s^{-1} . To ensure that our spectra of the LMC objects are similar to those typically obtained from objects in more distant galaxies, we scanned the slit across each entire LMC object, in order to obtain “global” spectra. In a few cases, we also obtained simple long-slit spectra at a single position to compare with our scans. We also obtained a few spectra of SNRs and H II regions in M83 as a preliminary test of this technique for a more distant galaxy. Our conclusions are as follows:

- Spectroscopy with $\sim 50 \text{ km s}^{-1}$ resolution is indeed an effective way to separate SNRs from H II regions, even for the largest LMC SNRs in our sample. The typical Gaussian velocity widths of the SNRs are $\sim 130 \text{ km s}^{-1}$ (FWHM)⁵ whereas the H II region lines appear near the instrumental resolution of $\sim 50 \text{ km s}^{-1}$.
- The widths of lines in the “global” (scanned) spectra are generally larger than the lines in corresponding simple long-slit spectra, because of bulk velocity shifts in the various portions of the SNR. The velocity widths of the lines in our spectra from H α , [N II], and [S II] are all similar for objects with little contaminating H II region emission. For the M83 SNRs, such contamination does seem to affect H α more than the [N II] and [S II] lines, making these forbidden lines that are typically strong in SNRs somewhat more effective as the kinematic diagnostic.
- The integrated H α luminosity for LMC SNRs ranges up to at least $3 \times 10^{37} \text{ erg s}^{-1}$, somewhat higher than for M31 or M33 SNRs, and approaching the values found in the starburst galaxy M83.
- While the smaller diameter SNRs often have higher velocity widths in their global spectra, there is considerable scatter at small diameter, consistent with the idea that density (and possibly explosion energy) strongly affect the appearance of SNRs at the same diameter.

In summary, we believe that kinematics provide a clean way to discriminate between SNRs and H II regions at optical wavelengths. We plan, and encourage others, to pursue higher resolution spectroscopy of the various SNR samples in nearby galaxies as a way of resolving the uncertain identifications of objects, especially those near the often-used [S II]:H α = 0.4 boundary where the largest uncertainty lies. This will result in more complete, less contaminated samples of *bona fide* SNRs, which are needed for understanding the global properties of SNRs and their impact on their host galaxies.

This work was based on observations obtained at the Southern Astrophysical Research (SOAR) telescope, which is a joint project of the Ministério da Ciência, Tecnologia, Inovações e Comunicações (MCTIC) do Brasil, the U.S. National Optical Astronomy Observatory (NOAO), the University of North Carolina at Chapel Hill (UNC), and Michigan State University (MSU). SDP would like to thank P. Ugarte, C. Corco, and S. Pizarro for their help at the telescope without which these observations would not have been possible. PFW acknowledges support from the NSF through grant AST-1714281. WPB thanks the Center for Astrophysical Sciences at Johns Hopkins University for support.

Facility: SOAR (Goodman)

REFERENCES

Blair, W. P., & Long, K. S. 1997, ApJS, 108, 261,

⁵ This is the median value of the H α widths as measured from the Gaussian fits. doi: [10.1086/312958](https://doi.org/10.1086/312958)

- . 2004, *ApJS*, 155, 101, doi: [10.1086/423958](https://doi.org/10.1086/423958)
- Blair, W. P., Winkler, P. F., & Long, K. S. 2012, *The Astrophysical Journal Supplement Series*, 203, 8, doi: [10.1088/0067-0049/203/1/8](https://doi.org/10.1088/0067-0049/203/1/8)
- Bozzetto, L. M., Filipović, M. D., Vukotić, B., et al. 2017, *ApJS*, 230, 2, doi: [10.3847/1538-4365/aa653c](https://doi.org/10.3847/1538-4365/aa653c)
- Clemens, J. C., Crain, J. A., & Anderson, R. 2004, in *Society of Photo-Optical Instrumentation Engineers (SPIE) Conference Series*, Vol. 5492, Proc. SPIE, ed. A. F. M. Moorwood & M. Iye, 331–340
- Davies, R. D., Elliott, K. H., & Meaburn, J. 1976, *MmRAS*, 81, 89
- de Vaucouleurs, G., Pence, W. D., & Davoust, E. 1983, *ApJS*, 53, 17, doi: [10.1086/190881](https://doi.org/10.1086/190881)
- D’Odorico, S., Benvenuti, P., & Sabbadin, F. 1978, *A&A*, 63, 63
- Ghavamian, P., Seitzzahl, I. R., Vogt, F. P. A., et al. 2017, *ApJ*, 847, 122, doi: [10.3847/1538-4357/aa83b8](https://doi.org/10.3847/1538-4357/aa83b8)
- Gordon, S. M., Kirshner, R. P., Long, K. S., et al. 1998, *ApJS*, 117, 89, doi: [10.1086/313107](https://doi.org/10.1086/313107)
- Green, D. A. 2017, *VizieR Online Data Catalog*, VII/278
- Haffner, L. M., Reynolds, R. J., & Tufte, S. L. 1999, *ApJ*, 523, 223, doi: [10.1086/307734](https://doi.org/10.1086/307734)
- Hamuy, M., Suntzeff, N. B., Heathcote, S. R., et al. 1994, *PASP*, 106, 566
- Hamuy, M., Walker, A. R., Suntzeff, N. B., et al. 1992, *PASP*, 104, 533
- Heng, K. 2010, *PASA*, 27, 23, doi: [10.1071/AS09057](https://doi.org/10.1071/AS09057)
- Henize, K. G. 1956, *ApJS*, 2, 315, doi: [10.1086/190025](https://doi.org/10.1086/190025)
- Hughes, J. P., Hayashi, I., Helfand, D., et al. 1995, *ApJL*, 444, L81, doi: [10.1086/187865](https://doi.org/10.1086/187865)
- Lee, J. H., & Lee, M. G. 2014a, *ApJ*, 786, 130, doi: [10.1088/0004-637X/786/2/130](https://doi.org/10.1088/0004-637X/786/2/130)
- . 2014b, *ApJ*, 793, 134, doi: [10.1088/0004-637X/793/2/134](https://doi.org/10.1088/0004-637X/793/2/134)
- Lee, M. G., Sohn, J., Lee, J. H., et al. 2015, *ApJ*, 804, 63, doi: [10.1088/0004-637X/804/1/63](https://doi.org/10.1088/0004-637X/804/1/63)
- Long, K. S. 2017, *Galactic and Extragalactic Samples of Supernova Remnants: How They Are Identified and What They Tell Us*, 2005
- Long, K. S., Blair, W. P., Milisavljevic, D., Raymond, J. C., & Winkler, P. F. 2018, *ApJ*, 855, 140, doi: [10.3847/1538-4357/aaac7e](https://doi.org/10.3847/1538-4357/aaac7e)
- Long, K. S., Winkler, P. F., & Blair, W. P. 2019, *ApJ*, 875, 85, doi: [10.3847/1538-4357/ab0d94](https://doi.org/10.3847/1538-4357/ab0d94)
- Long, K. S., Blair, W. P., Winkler, P. F., et al. 2010, *ApJS*, 187, 495, doi: [10.1088/0067-0049/187/2/495](https://doi.org/10.1088/0067-0049/187/2/495)
- Maddox, L. A., Cowan, J. J., Kilgard, R. E., et al. 2006, *AJ*, 132, 310, doi: [10.1086/505024](https://doi.org/10.1086/505024)
- Maggi, P., Haberl, F., Kavanagh, P. J., et al. 2016, *A&A*, 585, A162, doi: [10.1051/0004-6361/201526932](https://doi.org/10.1051/0004-6361/201526932)
- Massey, P., McNeill, R. T., Olsen, K. A. G., et al. 2007, *AJ*, 134, 2474, doi: [10.1086/523658](https://doi.org/10.1086/523658)
- Mathewson, D. S., & Healey, J. R. 1964, in *IAU Symposium*, Vol. 20, *The Galaxy and the Magellanic Clouds*, ed. F. J. Kerr, 283
- Matonick, D. M., & Fesen, R. A. 1997, *ApJS*, 112, 49, doi: [10.1086/313034](https://doi.org/10.1086/313034)
- Paredes, L., Points, S. D., Smith, R. C., et al. 2015, in *Astronomical Society of the Pacific Conference Series*, Vol. 491, *Fifty Years of Wide Field Studies in the Southern Hemisphere: Resolved Stellar Populations of the Galactic Bulge and Magellanic Clouds*, ed. S. Points & A. Kunder, 366–369
- Pietrzyński, G., Graczyk, D., Gieren, W., et al. 2013, *Nature*, 495, 76, doi: [10.1038/nature11878](https://doi.org/10.1038/nature11878)
- Saha, A., Thim, F., Tammann, G. A., Reindl, B., & Sandage, A. 2006, *ApJS*, 165, 108, doi: [10.1086/503800](https://doi.org/10.1086/503800)
- Smith, R. C., & MCELS Team. 1999, in *IAU Symposium*, Vol. 190, *New Views of the Magellanic Clouds*, ed. Y.-H. Chu, N. Suntzeff, J. Hesser, & D. Bohlender, 28
- Soria, R., & Wu, K. 2003, *A&A*, 410, 53, doi: [10.1051/0004-6361:20031074](https://doi.org/10.1051/0004-6361:20031074)
- Westerlund, B. E., & Mathewson, D. S. 1966, *MNRAS*, 131, 371, doi: [10.1093/mnras/131.3.371](https://doi.org/10.1093/mnras/131.3.371)
- Williams, R. M., Chu, Y.-H., Dickel, J. R., et al. 1999, *ApJS*, 123, 467, doi: [10.1086/313246](https://doi.org/10.1086/313246)
- Winkler, P. F., Blair, W. P., & Long, K. S. 2017, *ApJ*, 839, 83, doi: [10.3847/1538-4357/aa683d](https://doi.org/10.3847/1538-4357/aa683d)
- Winkler, P. F., Smith, R. C., Points, S. D., & MCELS Team. 2015, in *Astronomical Society of the Pacific Conference Series*, Vol. 491, *Fifty Years of Wide Field Studies in the Southern Hemisphere: Resolved Stellar Populations of the Galactic Bulge and Magellanic Clouds*, ed. S. Points & A. Kunder, 343

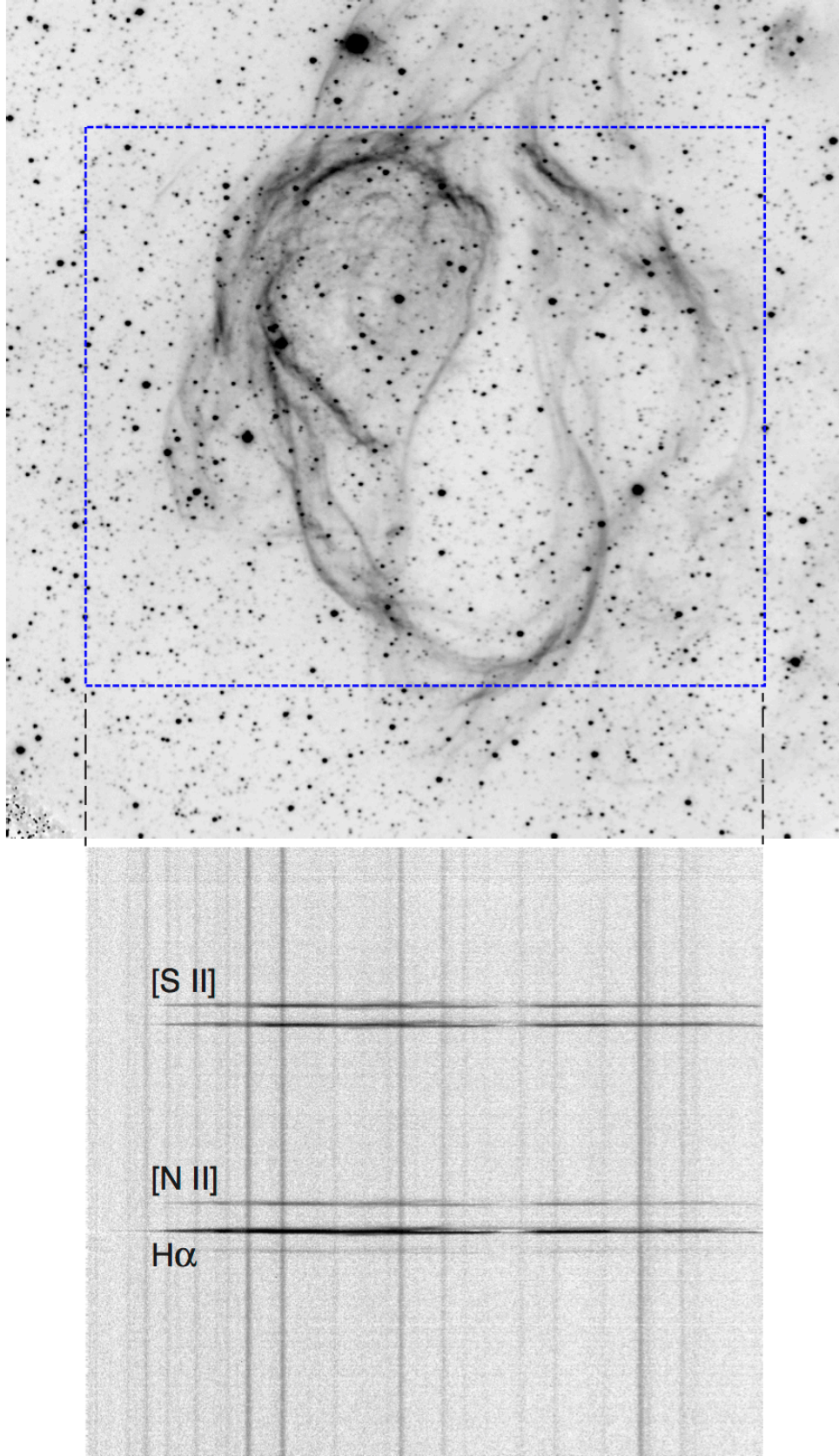


Figure 1. (*top*) An $H\alpha$ image of the LMC SNR N86 (J0455–6839) from the Goodman spectrograph in direct imaging mode. The field is $5'$ square and is oriented N up, E left. The blue dashed rectangle indicates the region scanned north to south using an E-W slit. (*bottom*) A portion of the sky-subtracted 2-D spectrum from the scan, displayed at the same spatial scale; black dashed lines in the upper figure indicate the ends of the slit. Complex velocity structure, showing both blue- and red-shifts, is present in the nebular emission. The dark vertical traces are the signatures of brighter stars within the scan region, as seen in the image, directly above the spectroscopic traces. The 1-D extraction for N86 is shown as the second trace from the top in Fig. 4.

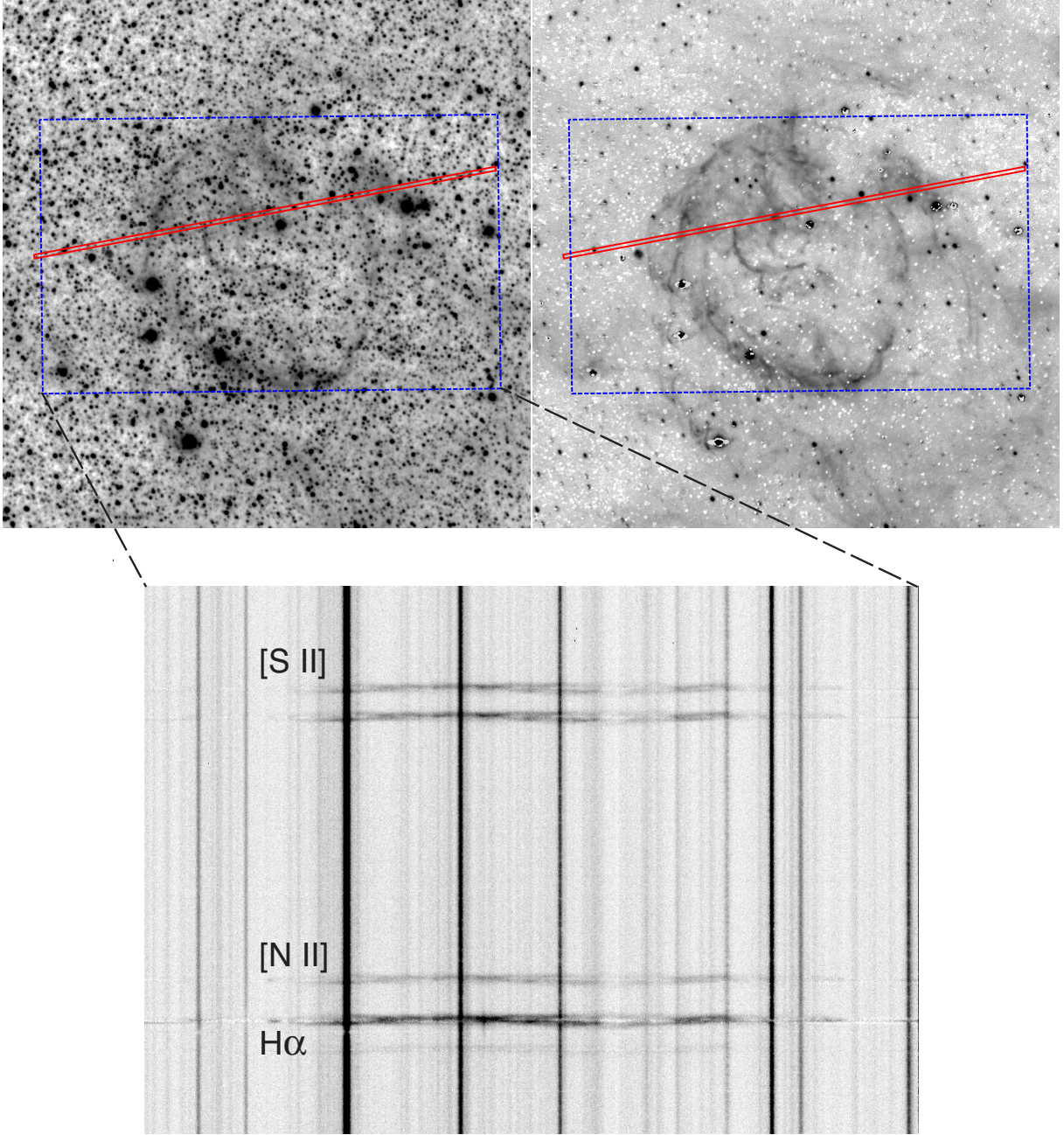


Figure 2. (*top panels*) $H\alpha$ images of the SNR B0520–69.4 = J0519–6926, located in the densely populated bar of the LMC. The left image is before continuum subtraction, and the one to the right is after. The field is 4.5 square, oriented N up, E left. The blue dashed rectangle indicates the region scanned north-to-south using an E-W slit. For this object we also obtained a long-slit spectrum at the position indicated in red. (*bottom*) A portion of the 2-D spectrum from the scan over the region indicated above. Complex velocity structure along the slit is obvious. The 1-D spectrum extracted from this 2-D one is shown as the lower trace of Fig. 3.

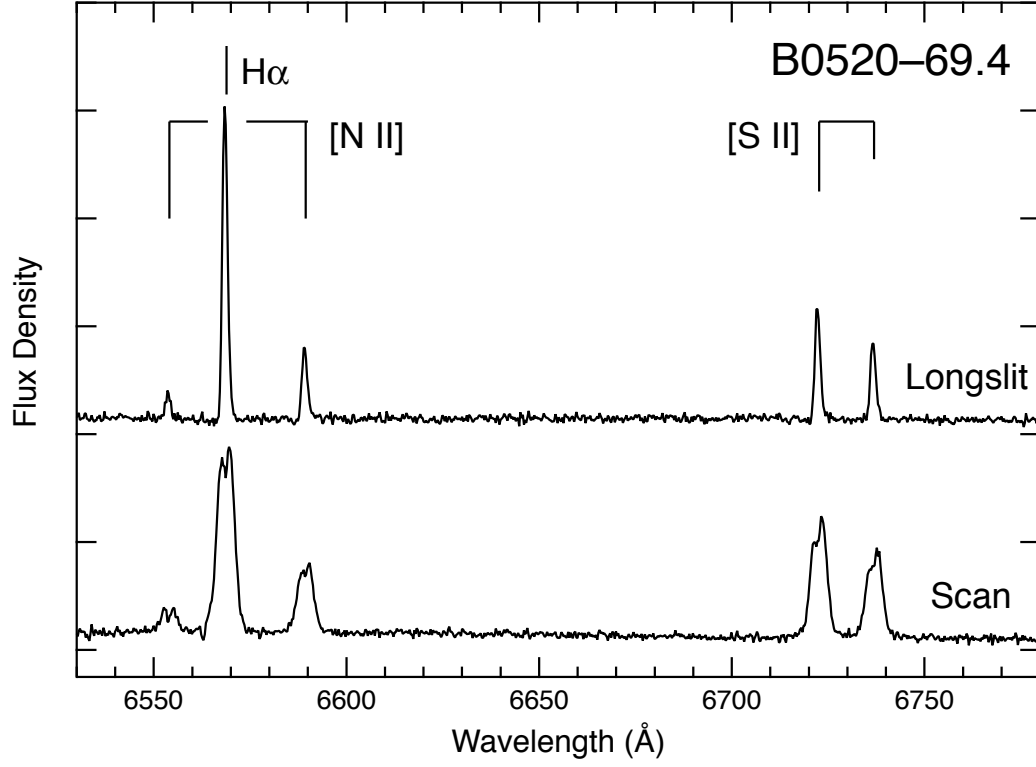


Figure 3. The lower trace shows the 1-D spectrum of the SNR B0520-69.4 = J0519-6926 obtained by summing over the spatial direction in 2-D spectrum from a scan of the entire object (Fig. 2, bottom panel), while the upper trace shows a similar extraction from a long-slit 2-D spectrum at the position indicated on the upper panels of Fig. 2. The scan clearly shows more velocity structure and broader lines than the long-slit data.

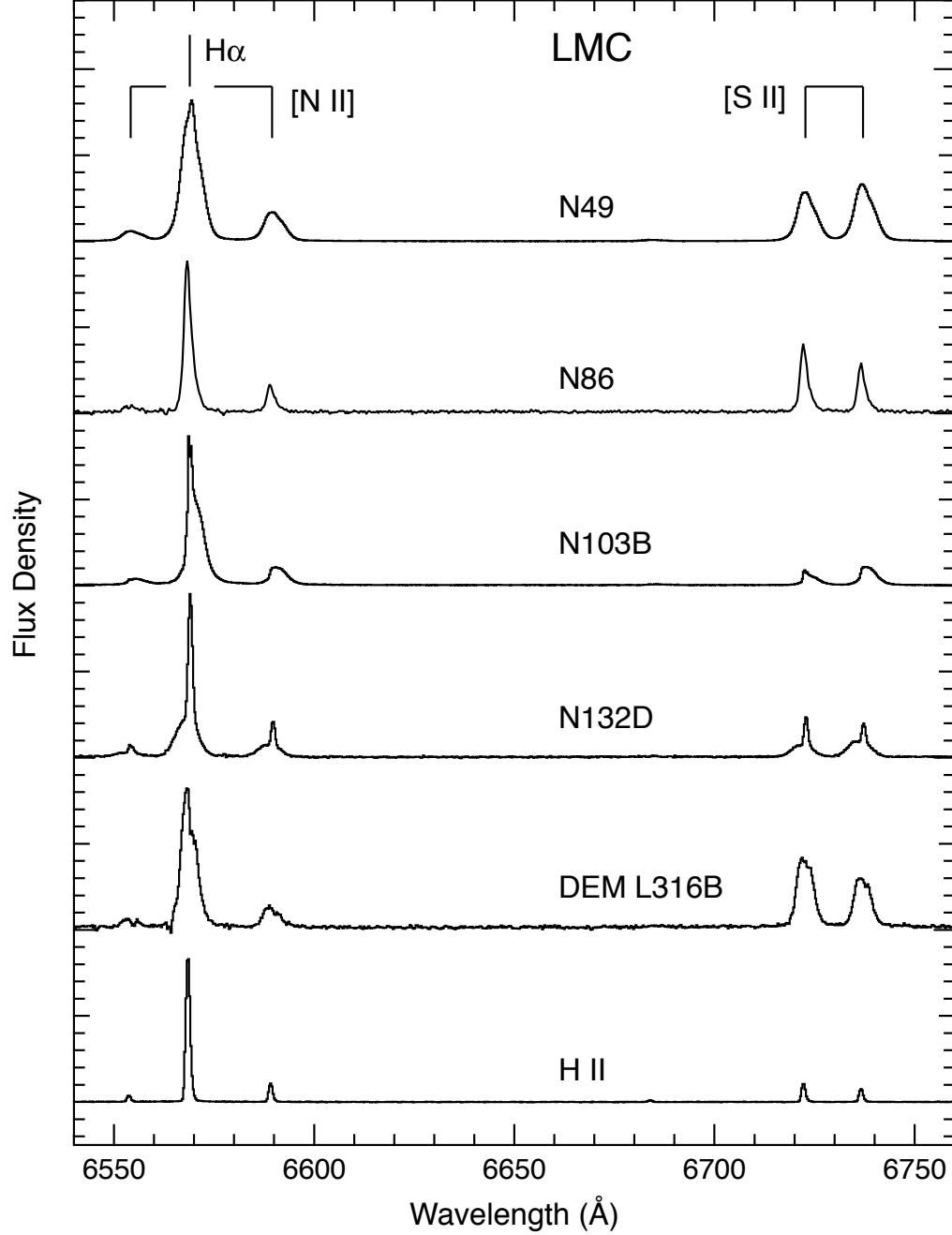


Figure 4. Sections from the 1-D spectra for five SNRs and one H II region, all in the LMC (arbitrarily scaled). All are the result of scanned 2-D spectra that have been sky-subtracted, and then summed over the extent of the object to give the 1-D spectra shown here. All of the SNRs have lines that are noticeably broader than those in the H II region shown, as well as in other H II regions that we studied. Note that for N103B, the global [S II]:H α ratio is less than the canonical value of 0.4 for SNRs, and also that there is a narrow component to the H α line. Both are due to overlying/contaminating H II emission.

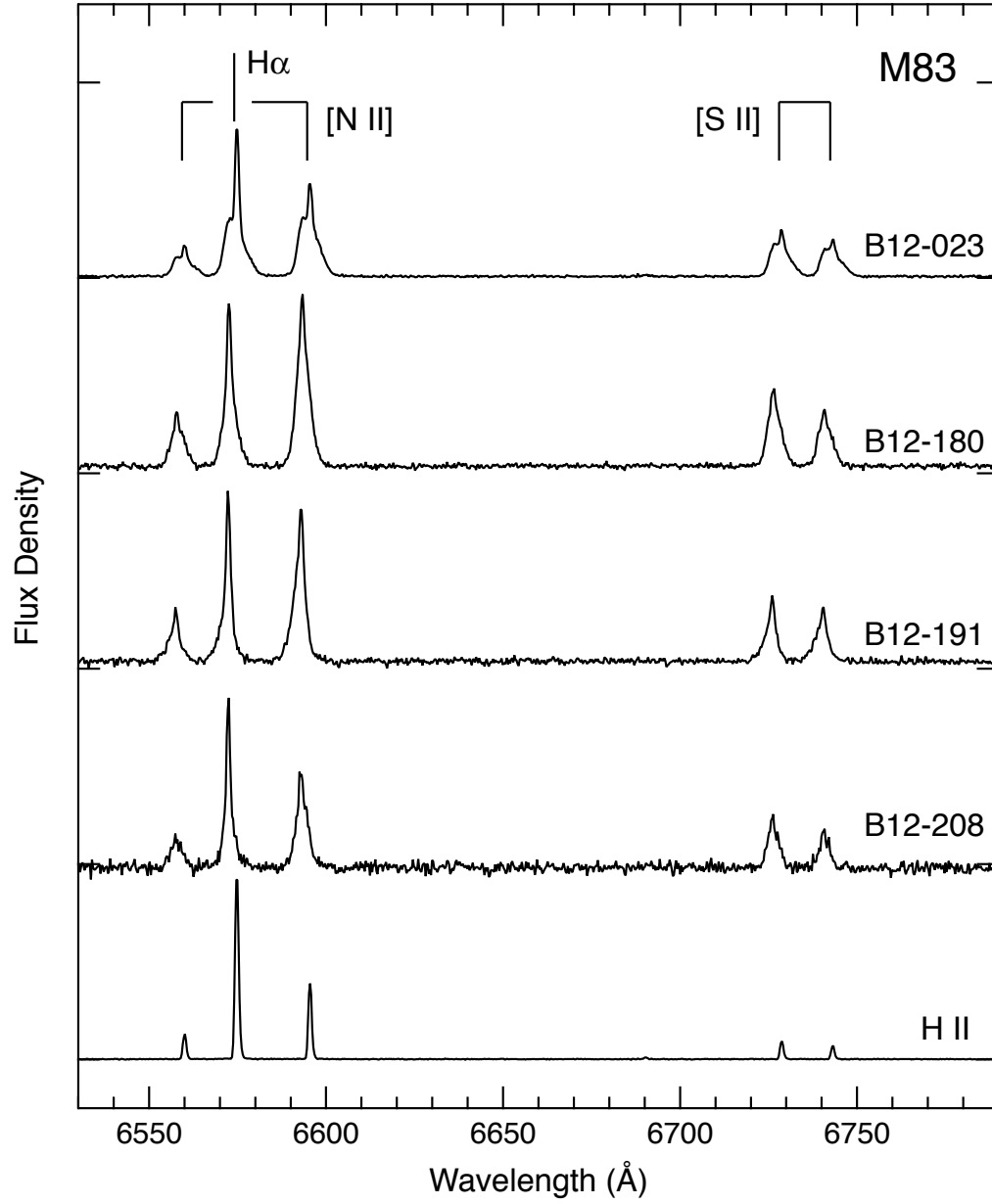


Figure 5. Sections from the long-slit spectra for four SNRs in M83, plus an H II region for comparison. All the SNRs have [S II]:H α ratios > 0.4 , as expected, and all show significantly broadened lines as well. The lines from the H II region are consistent with the $\sim 53 \text{ km s}^{-1}$ instrumental resolution of the Goodman spectrograph in the setup we used.

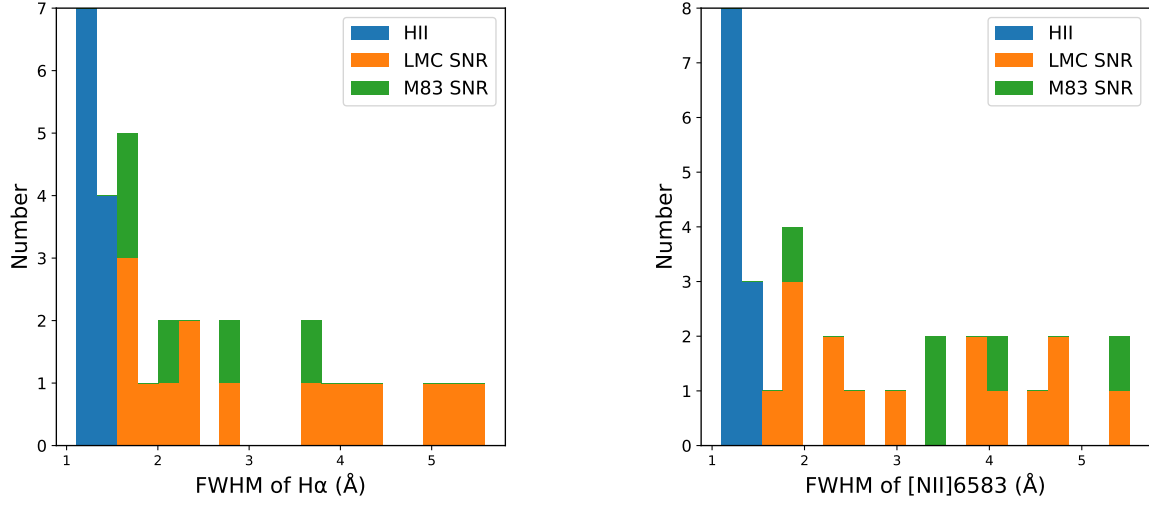


Figure 6. Histograms of the widths of the $H\alpha$ (left) and $[N II] \lambda 6583$ lines in H II region spectra compared to SNR spectra in the LMC and M83. Even though the H II region lines are not fully resolved, the larger values for the SNRs is clear.

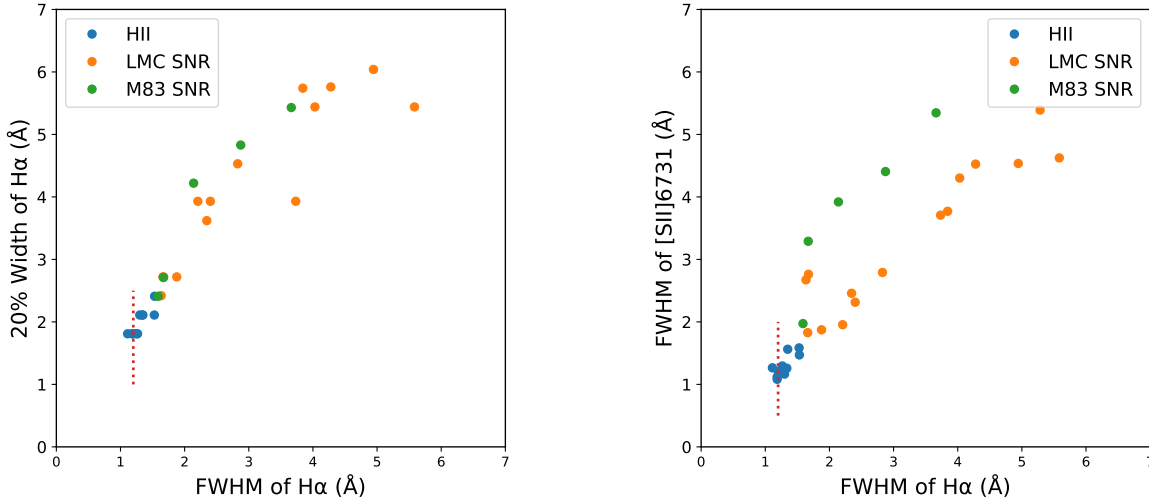


Figure 7. Left: A comparison between the width of the lines measured by Gaussian fitting and the width measured at the 20% of peak level. Right: A comparison between the widths measured by Gaussian fits in $H\alpha$ compared to one of the $[S II]$ lines. For the LMC SNRs, only the scanned spectra are shown. The dotted line at 1.2\AA indicates the FWHM of the instrumental resolution. Note the systematically broader $[S II]$ lines compared with $H\alpha$ for the M83 objects in the right panel.

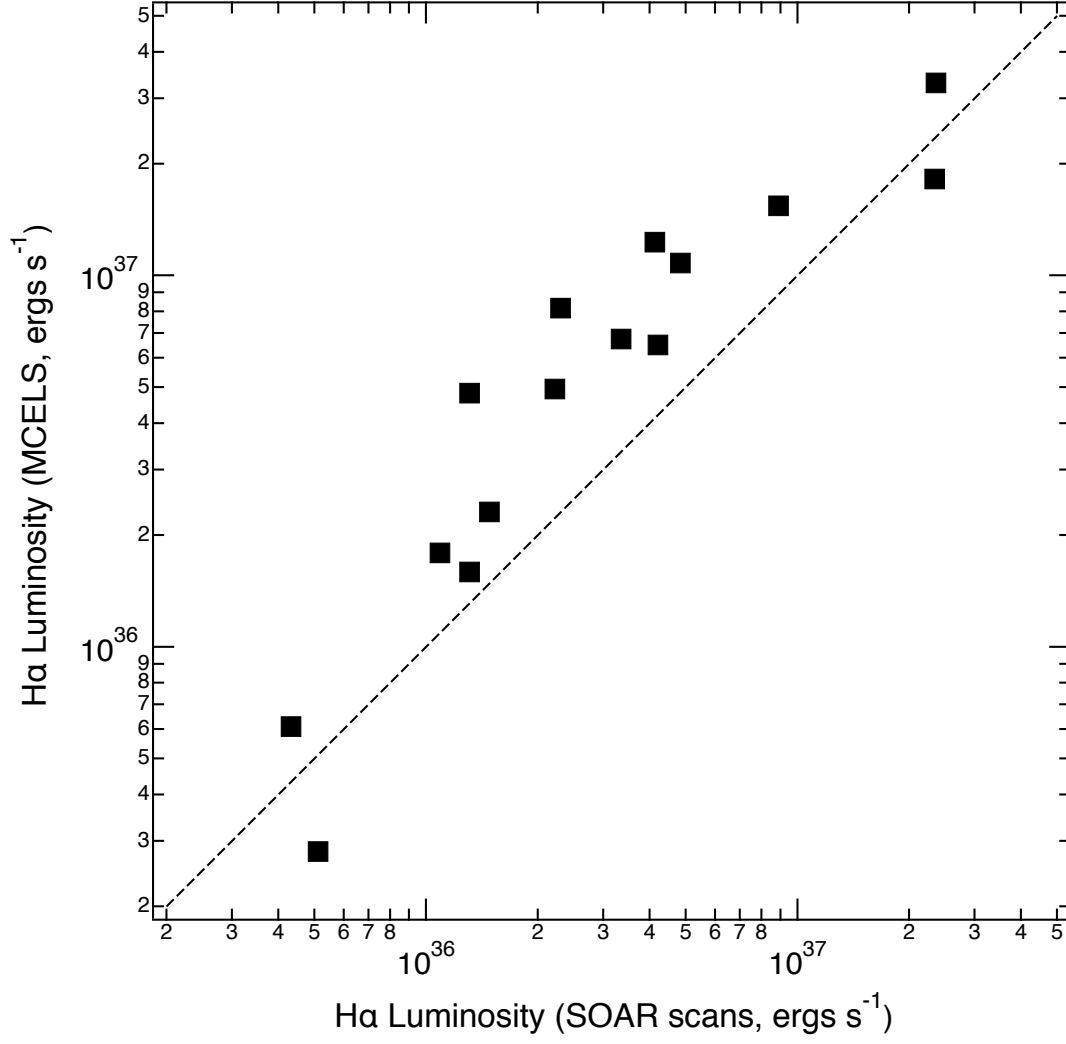


Figure 8. Comparison of the H α luminosity for LMC SNRs in our sample, based on integrated flux from our scanned spectra (horizontal axis), with measurements from the MCELS continuum-subtracted H α mosaic (vertical axis). The luminosities assume a distance of 50 kpc and negligible absorption.

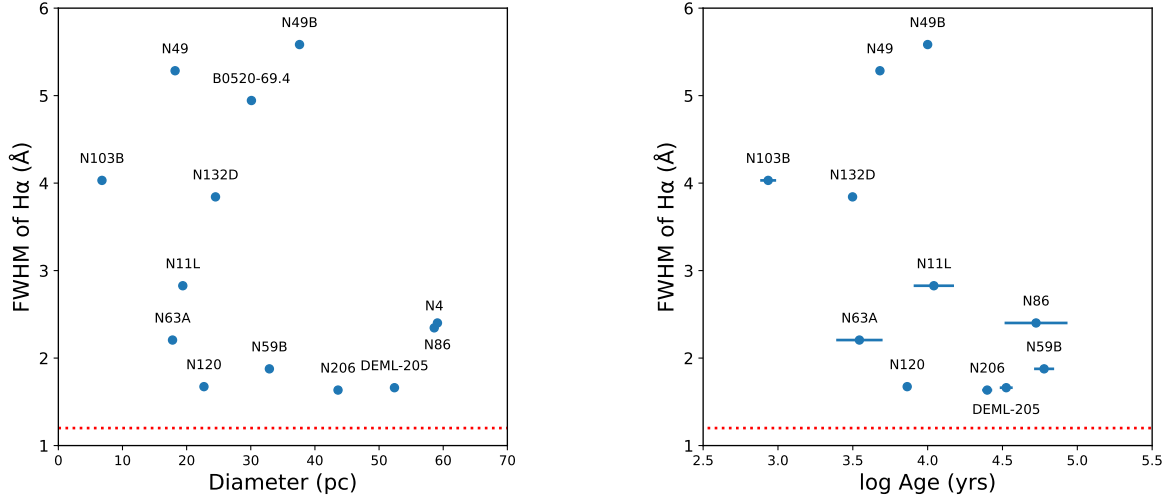


Figure 9. Left: The measured Gaussian FWHM of H α as a function of SNR diameter. Right: The H α Gaussian FWHM as a function of the age. Data for both x-axes, including errors on the age estimates, if available, are as compiled by [Bozzetto et al. \(2017\)](#). As in Fig. 7, the dotted line shows the instrumental resolution of 1.2 \AA .